scientific reports

OPEN

Nanostrucutured MnO$_2$-TiN nanotube arrays for advanced supercapacitor electrode material

Peng Ren[1,3], Chao Chen[2] & Xiuchun Yang[1,3,4]✉

The capacitance of MnO$_2$ supercapacitors (SCs) is not high as expected due to its low conductivity of MnO$_2$. The synergistic effects of MnO$_2$ with high theoretical specific capacitance and TiN with high theoretical conductivity can extremely enhance the electrochemical performance of the MnO$_2$-TiN electrode material. In this work, we synthesized different nanostructured and crystalline-structured MnO$_2$ modified TiN nanotube arrays electrode materials by hydrothermal method and explained the formation mechanism of different nanostructured and crystalline-structured MnO$_2$. The influences of MnO$_2$ nanostructures and crystalline-structures on the electrochemical performance has been contrasted and discussed. The specific capacitance of δ-MnO$_2$ nanosheets-TiN nanotube arrays can reach 689.88 F g^{-1}, the highest value among these samples TN-MO-SS, TN-MO-S, TN-MO-SR, TN-MO-RS, and TN-MO-R. The reason is explained based on MnO$_2$ nanostructure and crystalline-structure and electron/ion transport properties. The specific capacitance retention rates are 97.2% and 82.4% of initial capacitance after 100 and 500 cycles, respectively, indicating an excellent charging-discharging cycle stability.

With the development of renewable energy, high-performance electrochemical energy storage will take into account in the future. A device with an energy storage function called "Laihton bottle" was discovered by Dutch in 1746[1]. Since then, the mystery of capacitors has been gradually revealed. The research on supercapacitors(SCs) can be traced back to 1879 when Helmholz first discovered the characteristics of electric double-layer capacitance at the electrochemical interface[2]. In 1957, Becker applied for the first carbon electrode supercapacitor patent, which has a similar energy density to batteries and has a specific capacitance that is 3 to 4 orders of magnitude higher than ordinary capacitors[3]. In the researches on SCs, the electrode materials have an important effect on performance.

Generally, SCs can be divided into electrical double-layer capacitors (EDLCs) and pseudocapacitors (PCs) depending on their energy storage mechanism[4], EDLCs mainly based on high surface area materials, such as carbon, graphene[5], graphite oxide[6] so on, which are all kinds of nanostructures, PCs mainly based on metal oxides and graphene-like layered metal compounds[7], using transition metal oxide (Co$_3$O$_4$, NiO, RuO$_2$ and MnO$_2$, etc.) nanomaterials with good electrochemical properties is a practical way to optimize the electrochemical performance of the electrode materials for the development of high-performance SCs[8].

MnO$_2$ is considered as a potential electrode material for SCs, which not only possesses electric double layer capacitance but also has high pseudocapacitance capacity as a semiconductor. The theoretical specific capacitance of MnO$_2$ can reach 1370 F g^{-1}[9,10]. In 1999, Lee and Goodenough first researched the pseudocapacitance properties of MnO$_2$ in an aqueous solution and proposed that the main energy storage mechanism is the pseudocapacitance reaction in the electrode material[11]. The charge/discharge processes mainly include the adsorption/desorption of metal cations on the surface of MnO$_2$ and the intercalation/de-intercalation in MnO$_2$ with rapid and reversible redox reactions[12,13]. In addition, the crystal structure of MnO$_2$ directly impacts electrochemical performance. Brousse et al. prepared MnO$_2$ with different crystal structures and studied their electrochemical properties[14]. The results showed that the specific capacitances of one-dimensional α-MnO$_2$ and two-dimensional δ-MnO$_2$ are about 110 F g^{-1}, respectively. Ghodbane et al. further studied MnO$_2$ electrode materials with different crystal structures and proposed that the specific capacitances of the λ-MnO$_2$ and δ-MnO$_2$ with three-dimensional structures are 241 F g^{-1} and 225 F g^{-1}, respectively[15]. The capacitance of the SCs with simple MnO$_2$ electrode is not high

[1]Shanghai Key Laboratory of R&D for Metallic Functional Materials, Tongji University, Shanghai 201804, People's Republic of China. [2]School of Chemistry and Civil Engineering, Shaoguan University, Shaoguan 512005, People's Republic of China. [3]Key Laboratory of Advanced Civil Engineering Materials of Ministry of Education, Tongji University, Shanghai 201804, People's Republic of China. [4]School of Materials Science and Engineering, Tongji University, Shanghai 201804, People's Republic of China. ✉email: yangxc@tongji.edu.cn

Solution	KMnO$_4$	MnSO$_4$·H$_2$O	HCl	H$_2$O	Temperature [°C]	Time [h]	Sample
M-1	0.875 g	0.35 g	–	70 mL	140	3	TN-MO-SS
						12	TN-MO-S
						18	TN-MO-SR
M-2	1.106 g	–	0.88 mL	70 mL	150	6	TN-MO-RS
M-3	0.7875 g	–	1.75 mL	70 mL	150	12	TN-MO-R

Table 1. The precursor solution compositions and conditions of hydrothermal reaction for preparing nanostructured MnO$_2$.

as expected due to the low conductivity of MnO$_2$ ($10^{-3} \sim 10^{-4}$ S m^{-1})[16]. Therefore, MnO$_2$ needs to be compounded with other materials with good electrical conductivity to improve the overall electrochemical performance including specific capacitance, charge/discharge performance, and cycle characteristics, researchers have made many attempts to prepare supercapacitor electrodes by mixing MnO$_2$ with highly conductive materials[17–24], Since transition metal nitrides have great electrical conductivity, electrochemical characteristics, chemical stability and long service life, TiN, VN, WN, CrN and TiVN are widely used as electrode materials of SCs[25–27]. TiN has been used in electric devices such as microelectronics, semiconductor device electrodes, lithium ion batteries, fuel cells and SCs as a low-cost transition metal nitride with good conductivity (4000 $\sim$ 55,500 s cm^{-1}) and stability[28–30]. Tang et al. used urea and TiCl$_4$ to prepare TiN as a SCs electrode material with a specific capacitance of 407 F g^{-1}[31].

In this work, MnO$_2$ nanosheet spheres, nanosheets, nanorod spheres, and nanorods are synthesized on TiN nanotube arrays for obtaining an electrode material for SCs, where the nanostructured MnO$_2$ is more chemically stable than MoS$_2$[32] and has better electrochemical performance than layered MnO$_2$[33]. The composition and morphology are measured by using XRD, SEM and EDS. The electrochemical performances of all samples in an electrolyte containing K$^+$ are measured and discussed.

Methods

Preparation of TiO$_2$ NTAs on mesh (TONM). All reagents are analytical grade and used without further purification. A large piece of raw Ti mesh (50 meshes, 99.5% purity) with a thickness of 0.12 mm was cut into square pieces of 2.5 × 2.5 cm^2, which were ultrasonically degreased in acetone, isopropanol, and methanol for 15 min, respectively, then chemically etched in a mixture of HF and HNO$_3$ aqueous solution (HF:HNO$_3$:H$_2$O = 1:4:10 in volume, total 20 mL) for 10 s, afterward rinsed with deionized water and finally dried in air. Electrochemical anodic oxidation was performed at 60 V direct current voltages for 24 h in DEG solution containing 1.5 vol.% HF, using Ti mesh as the working electrode and Pt plate as a counter electrode. The as-prepared samples were ultrasonically rinsed with deionized water and dried in the air[33].

Preparation of TiN NTAs on mesh (TNNM). TONM samples in a quartz boat were placed in the heating center of a horizontal quartz tube vacuum furnace. Prior to heating, the system was evacuated and flushed with high pure N$_2$ to eliminate oxygen. Afterward, the furnace was heated in N$_2$ to 750 °C, and then changed to NH$_3$ flow keeping a flow rate of 100 mL/min for 5 h while the temperature was maintained. Finally, the furnace cooled down to room temperature in N$_2$.

Preparation of MnO$_2$ modified TNNM. Different precursor solutions were employed for synthesizing MnO$_2$ nanostructures by hydrothermal synthesis method. A TNNM sample was placed at the bottom of the reaction solution in a sealed 150 mL Teflon-lined autoclave, which was put into a muffle furnace for hydrothermal reaction. The solution compositions and reaction solutions are summarized in Table 1.

Characterization. The crystalline phase compositions of the samples were measured by a Rigaku D/Max 2550VB3+/PC X-ray diffractometer (XRD) equipped with graphite monochromatized Cu Kα radiation (λ = 0.15405 nm). Nanostructures and elemental distributions of the samples were characterized by a Schottky field emission scanning electron microscopy (FESEM, FEI Nova NanoSEM 450) equipped with energy dispersive spectroscope (EDS, EDAX).

Electrochemical performance measurement. Electrochemical measurement was measured by CHI 660E electrochemical system using a three-electrode system where the samples as a working electrode, Pt foil as a counter electrode, and Ag/AgCl electrode as a reference electrode in 2 mol/L KCl solution. Cyclic voltammetry (CV) curves were obtained in a voltage range from − 0.2 V to 0.8 V at different scan rates of 5, 10, 20, 40, 60, 80 and 100 mV s^{-1}, respectively. Galvanostatic charge/discharge curves were recorded in a potential window from − 0.2 V to 0.8 V at a series of current densities. The electrochemical impedance spectroscopy (EIS) was conducted in the frequency from 100 kHz to 10 mHz at an open-circuit potential vibration of 5 mV[33].

Results and discussion

Figure 1a indicates that TNTM consists of Ti (JCPDS card No. 65-3362) and TiN (JCPDS card No. 65-5759). Ti is from Ti mesh and TiN is from the high-temperature ammonolysis of anodic TiO$_2$. Figure 1b indicates that the TiN is vertically aligned TiN nanotubes. As shown in the XRD patterns of TN-MO-SS, TN-MO-S, TN-MO-SR,
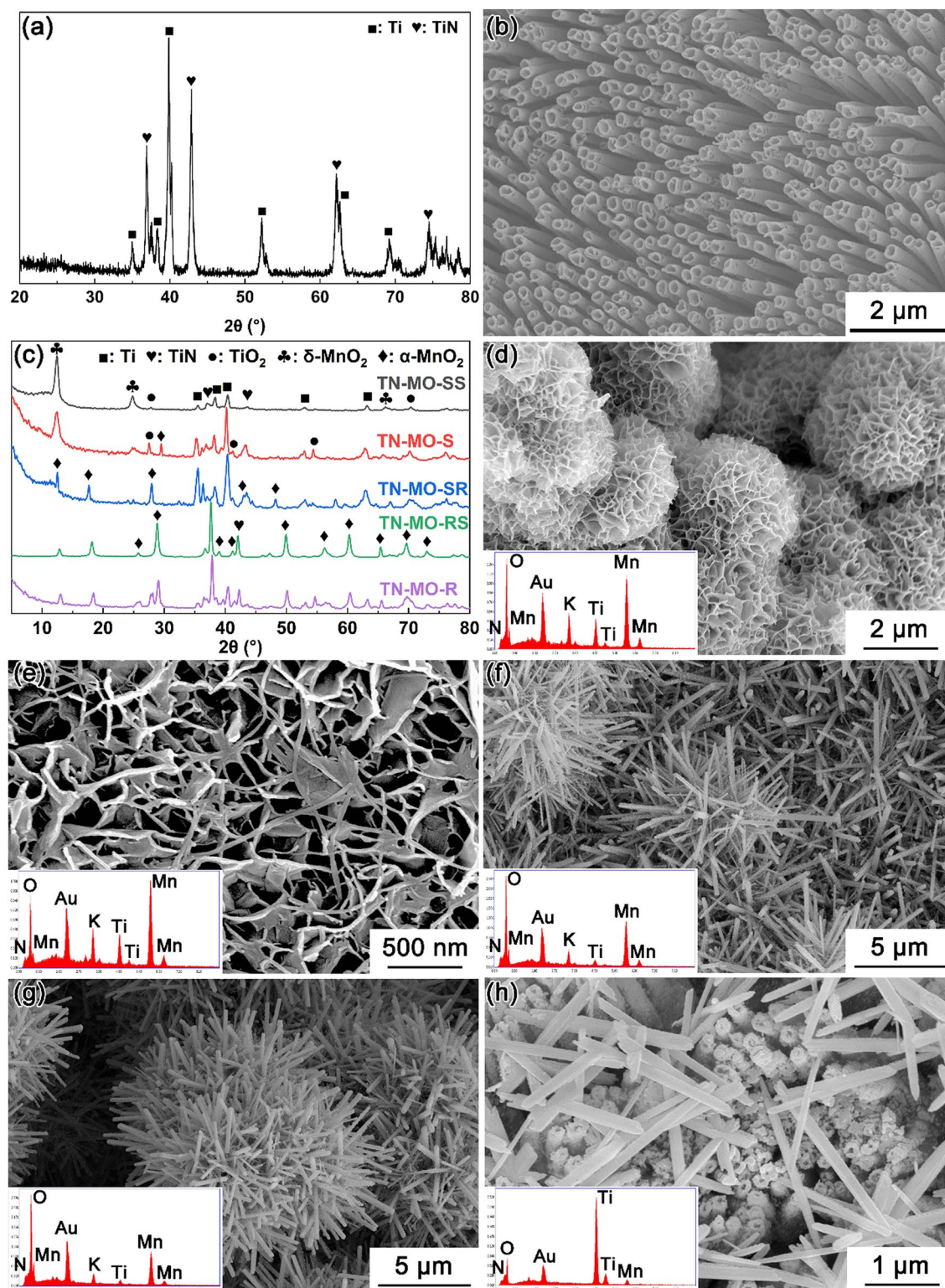
Figure 1. XRD pattern (**a**) and SEM image (**b**) of TNNM. XRD patterns (**c**) and SEM images (**d–h**, the insets are EDS spectra) of TN-MO-SS, TN-MO-S, TN-MO-SR, TN-MO-RS, and TN-MO-R.

TN-MO-RS, and TN-MO-R (Fig. 1c), TN-MO-SS and TN-MO-S mainly contain δ-MnO$_2$ crystals (JCPDS card No. 80-1098), while the MnO$_2$ in TN-MO-SR, TN-MO-RS, and TN-MO-R is α-MnO$_2$ (JCPDS card No. 44-0141). In addition, TN-MO-S also contains a little α-MnO$_2$. According to the SEM images in Fig. 1d–h, the MnO$_2$ nanostructures in TN-MO-SS, TN-MO-S, TN-MO-SR, TN-MO-RS and TN-MO-R are nanosheet spheres, nanosheets, nanorods, nanorod spheres and dispersed nanorods, respectively. The EDS spectra in Fig. 1d–h insets further demonstrate the compositions of all samples. Equations (1) and (2) depict the chemical reactions
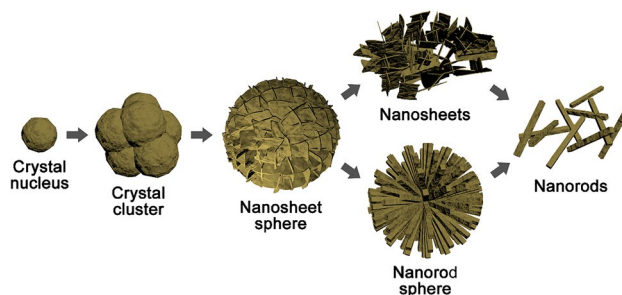
Figure 2. Schematic diagrams of MnO$_2$ nanostructure growth process.

for generating MnO$_2$ in M-1 (Eq. (1)), M-2 and M-3 (Eq. (2)) solutions[34,35]. Figure 2 shows the crystal growth process under hydrothermal reaction conditions. At first, a number of crystal nuclei rapidly form in the solution, which aggregates into nanoparticles. Afterward, nanosheets grow through the Ostwald ripening mechanism around the nanoparticles due to the particular lamellar crystal structure of δ-MnO$_2$ and the intercalation of K$^+$. As the hydrothermal reaction continues, the nanosheet spheres gradually disintegrate and form the intercalated nanosheets. Meanwhile, since α-MnO$_2$ is more stable than δ-MnO$_2$ thermodynamically, the δ-MnO$_2$ phase begins to transform into the α-MnO$_2$ phase with the α-MnO$_2$ nuclei generating in the δ-MnO$_2$ nanosheets. Then, the δ-MnO$_2$ crystal domains diffuse to the α-MnO$_2$ nucleus and convert into α-MnO$_2$, while α-MnO$_2$ nanorods grow through the Ostwald ripening mechanism[34,36]. In M-2 and M-3 solutions, the strong reducibility of Cl$^-$ and the presence of H$^+$ greatly accelerate the chemical reaction and phase transition speed[34].

$$3Mn^{2+} + 2MnO_4^- + 2H_2O \rightarrow 5MnO_2 + 4H^+ \tag{1}$$

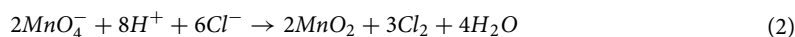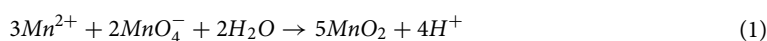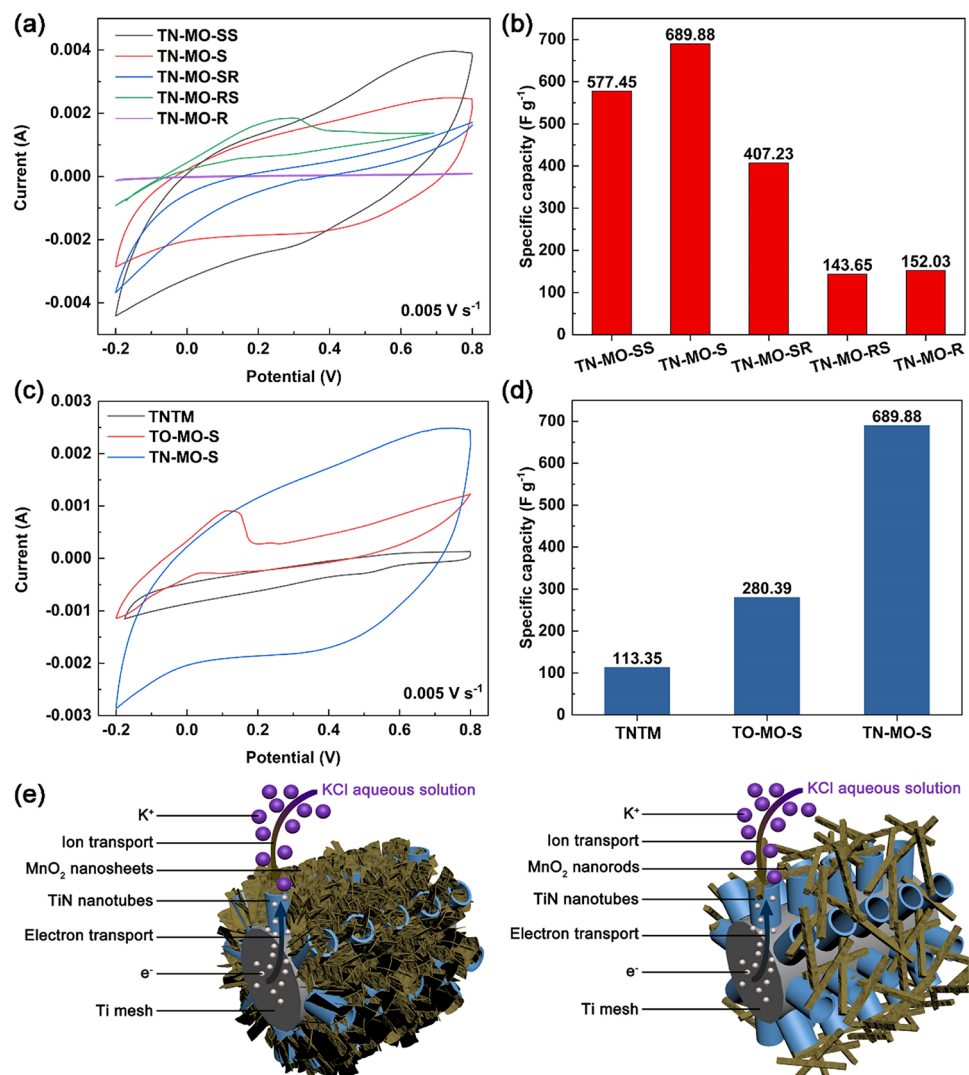$$2MnO_4^- + 8H^+ + 6Cl^- \rightarrow 2MnO_2 + 3Cl_2 + 4H_2O \tag{2}$$

Figure 3a,b show the cyclic voltammetry curves with the sweep speed of 5 mV s^{-1} and corresponding specific capacitances of samples TN-MO-SS, TN-MO-S, TN-MO-SR, TN-MO-RS, and TN-MO-R. TN-MO-S has the largest specific capacitance of 689.88 F g^{-1}. The specific capacitances of TN-MO-SS, TN-MO-SR, TN-MO-RS and TN-MO-R are 577.45 F g^{-1}, 407.23 F g^{-1}, 143.65 F g^{-1} and 152.03 F g^{-1}, respectively. Figure 3c,d show the cyclic voltammetry curves with the sweep speed of 5 mV s^{-1} and corresponding specific capacitances of TNTM, TO-MO-S and TN-MO-S. Obviously, the specific capacitance of TN-MO-S is about 6.1 times and 2.5 times of TNTM and TO-MO-S, respectively. The results demonstrate that the synergistic effects of MnO$_2$ nanosheets and TiN nanotube arrays significantly increase the specific capacitance. The specific capacitance mainly depends on the surface area of MnO$_2$ and the capacity of K^{+}[37]. TN-MO-S and TN-MO-SS have large specific surface area and great capacity for K$^+$ due to layered crystal structure (Fig. 4)[11]. The 3D structures formed by the intercalation of nanosheets benefit energy storage with electrolyte ions intercalation/de-intercalation and provide numerous chemical reaction sites. In addition, the contact between MnO$_2$ nanosheets and TiN nanotubes is more sufficient and tighter than that of MnO$_2$ nanorods, which facilitates the transport of electrons between the substrate and the active substance (Fig. 3e). Since the hydrothermal reaction time during the preparation of TN-MO-S is longer than TN-MO-SS, TN-MO-S contains more hydrates to adsorb more K$^+$ than TN-MO-SS, which further improves the pseudo-capacitance. TiN nanotube arrays can not only provide high-speed channels for electron transport, but also expands the specific surface area as a support for active substances providing more space for the ion intercalation/de-intercalation during the electrochemical process. Besides, TiN nanotube arrays directly contact with the substrate without the requirement of adhesion agent, which efficiently promotes the charge transfer between the interface.

Figure 5a,b show the curves and corresponding specific capacitance of TN-MO-S at different scan rates. The cyclic voltammetry curves maintain symmetrical shapes from 0.005 V s^{-1} to 0.1 V s^{-1}, indicating the magnification capacity of the electrode material. The specific capacitance decreases with the increase of scan rate because of the insufficient Faraday reaction time at a high scanning rate. Figure 5c shows the charging-discharging curves of TN-MO-S at different current densities. The nearly symmetrical triangular outlines manifest the capacitive and reversible characters of the electrode. The Nyquist plot, corresponding fitted curve and the equivalent circuit of TN-MO-S is shown in Fig. 5d. The internal resistance (R1) and the charge transfer resistance (R2) of the electrode are low as 1.183 Ω and 52.23 Ω, respectively, indicating excellent electronic conductivity and electron diffusion. Figure 5e depicts the cycle stability of TN-MO-S by charging-discharging measurements at a current density of 2 A g^{-1} for consecutive 500 cycles. The specific capacitance of the electrode maintains 97.2% and 82.4% of initial capacitance after 100 and 500 cycles, respectively. Figure 6 shows the composition and morphology of TN-MO-S after 500 charging-discharging measurement cycles. Generally, the composition and morphology hardly change as shown in Fig. 6a–c. Meanwhile, as shown in Fig. 6d,e, the amount of MnO$_2$ nanosheets deposited in some areas of the sample is reduced, indicating that the loss of the active substance is the main reason for the specific capacitance attenuation. However, it can be observed in Fig. 6d,e that MnO$_2$ nanosheets firmly and uniformly grow on not only the nanotube array surface but also the walls of nanotubes. The close integration of MnO$_2$

Figure 3. Cyclic voltammetry curves (**a**) and corresponding specific capacitances (**b**) of TN-MO-SS, TN-MO-S, TN-MO-SR, TN-MO-RS, and TN-MO-R with the sweep speed of 5 mV s⁻¹. Cyclic voltammetry curves (**c**) and corresponding specific capacitances (**d**) of TNNM, TO-MO-S and TN-MO-S with the sweep speed of 5 mV s⁻¹. Schematic diagrams of nanostructures of TN-MO-S and TN-MO-R (**e**).
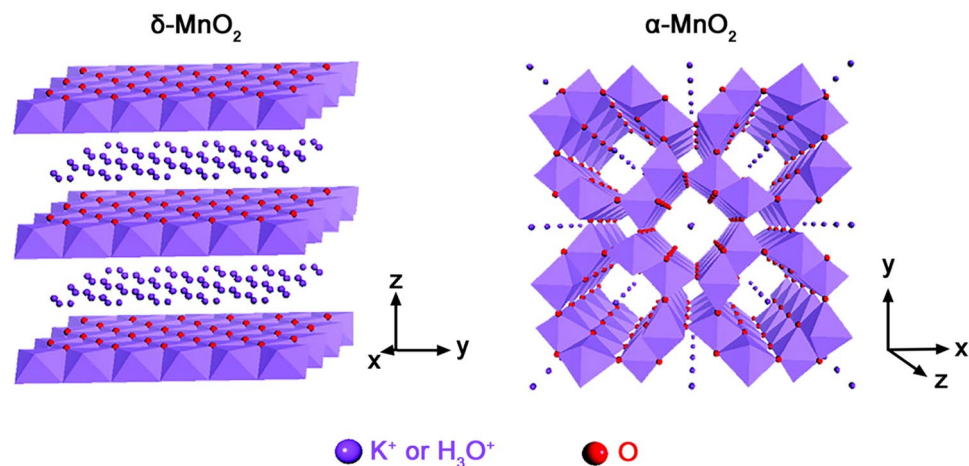
Figure 4. Schematic diagrams of δ-MnO$_2$ and α-MnO$_2$ crystal structure.
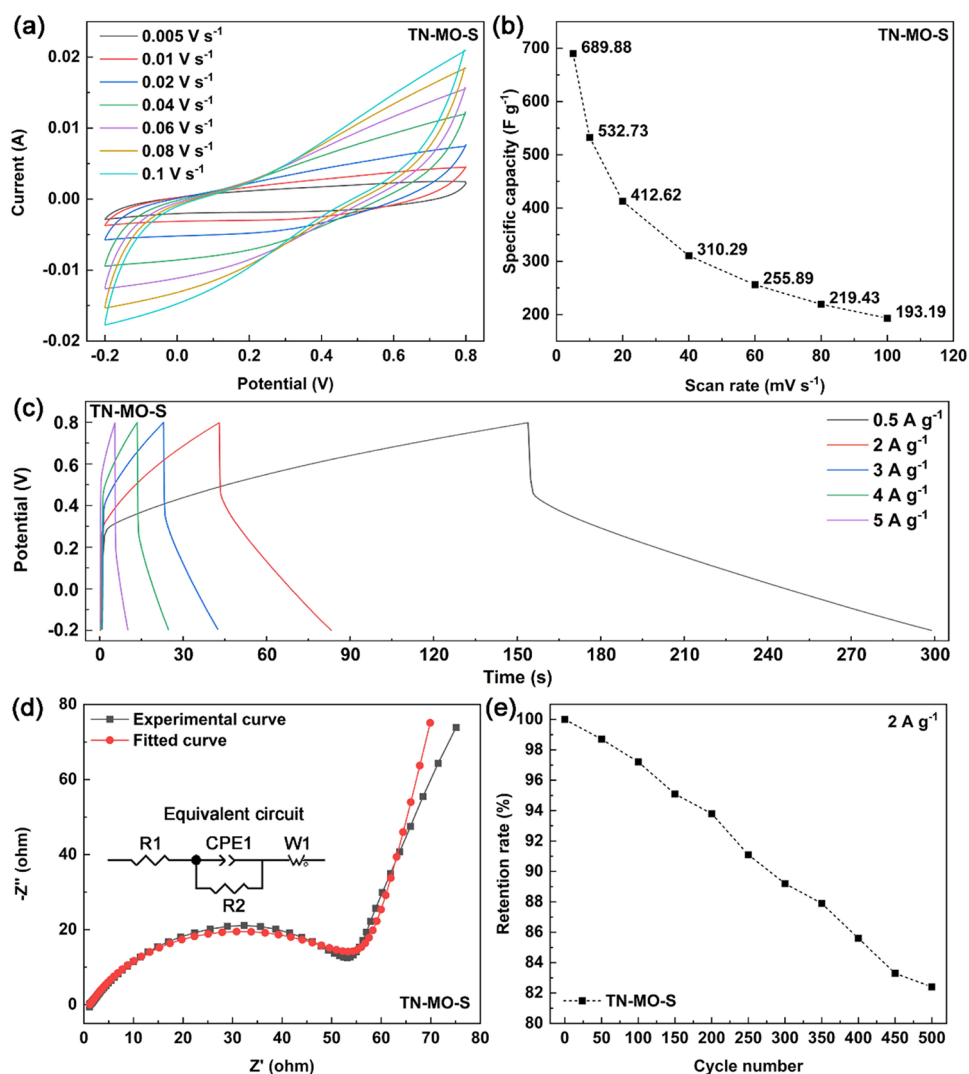
Figure 5. Cyclic voltammetry curves with different scan rates (**a**), corresponding specific capacitances (**b**), charge–discharge curves with different current densites (**c**), Nyquist plot and fitted curve (**d**, the inset shows the equivalent circuit), and the cyclic stability (**e**) of TN-MO-S.

nanosheets and TiN nanotubes improves the transportation of electrons and ions so that TN-MO-S has great electrochemical performance as a SCs electrode.

Conclusions

In summary, various MnO_2 nanostructures are synthesized on TiN nanotube arrays by hydrothermal method including nanosheet spheres, nanosheets, nanorod spheres, and nanorods for developing an advanced electrode material of SCs. The TiN nanotubes with excellent conductivity and great specific surface area provide highly efficient paths for charge transport and more electrochemical reaction sites. The nanostructured MnO_2 with high theoretical specific capacitance of 1370 F g^{-1} improves the pseudocapacitance reaction and specific capacitance of the electrode material. The specific capacitance of δ-MnO_2 nanosheets-TiN nanotube arrays can reach 689.88 F g^{-1} because of its good magnification capacity and its excellent electronic conductivity and electron/ion transport properties. Its specific capacitance retention rate is 97.2% and 82.4% of initial capacitance after 100 and 500 cycles, respectively, indicating a good charging-discharging cycle stability. Hence, the synergistic effect of TiN and MnO_2 can extremely enhance the electrochemical performance of the electrode material for SCs.
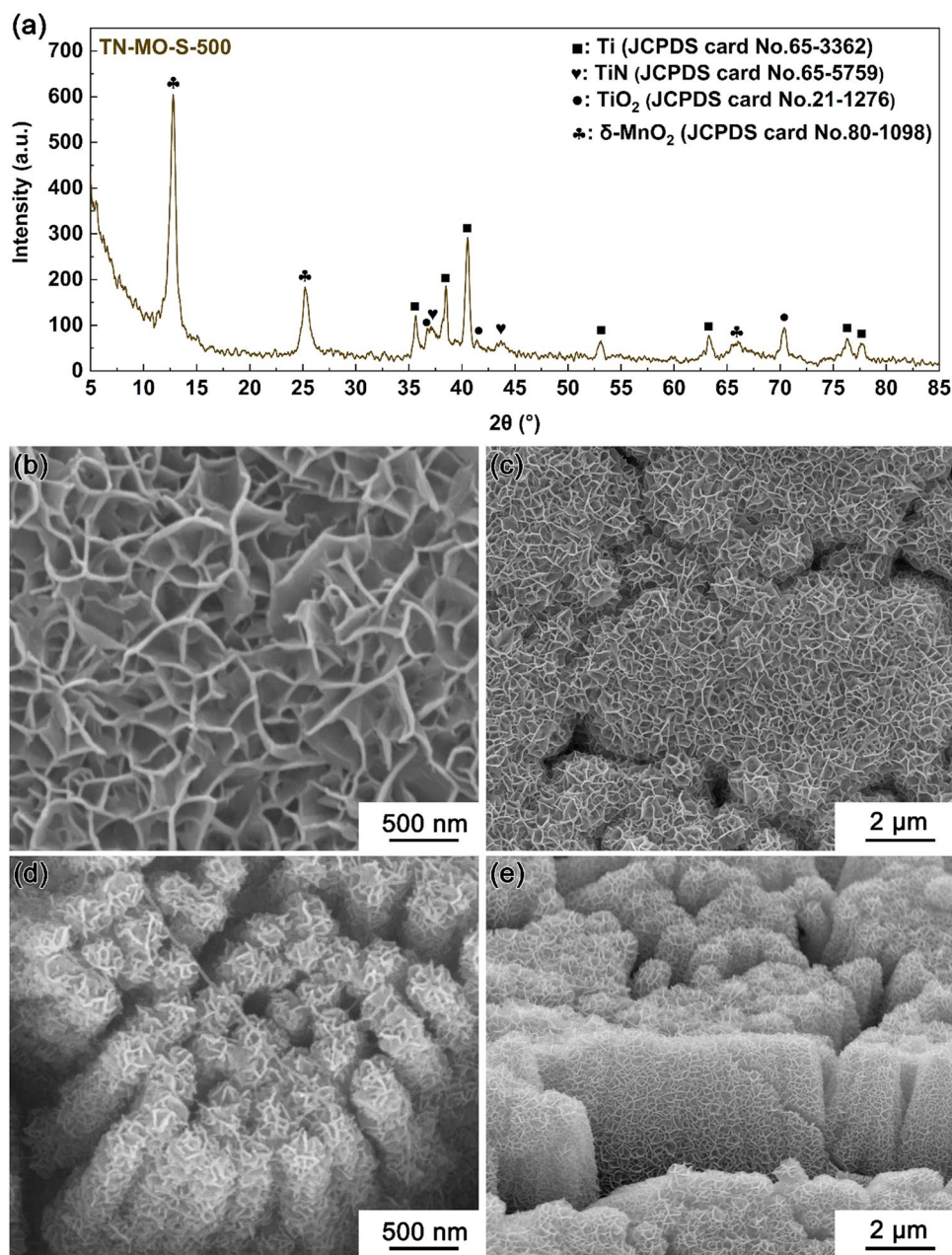
Figure 6. XRD pattern (**a**) and SEM images (**b**–**e**) of TN-MO-S-500.

Data availability
All data included in this study are available upon request by contact with the corresponding author.

References
1. Conway, B. E. Similarities and differences between supercapacitors and batteries for storing electrical energy. In *Electrochemical Supercapacitors* 11–31 (Springer, 1999).
2. Conway, B. E. & Pell, W. G. Double-layer and pseudocapacitance types of electrochemical capacitors and their applications to the development of hybrid devices. *J. Solid State Electrochem.* **7**, 637–644 (2003).
3. Lu, X., Yu, M., Wang, G., Tong, Y. & Li, Y. Flexible solid-state supercapacitors: Design, fabrication and applications. *Energy Environ. Sci.* **7**, 2160–2181 (2014).
4. Long, J. W. *et al.* Asymmetric electrochemical capacitors: Stretching the limits of aqueous electrolytes. *MRS Bull.* **36**, 513–522 (2011).
5. Li, Y. & Zhao, D. Preparation of reduced graphite oxide with high volumetric capacitance in supercapacitors. *Chem. Commun.* **51**, 5598–5601 (2015).

6. Kim, T. Y. *et al.* High-performance supercapacitors based on poly (ionic liquid)-modified graphene electrodes. *ACS Nano* **5**, 436–442 (2011).

7. Ren, Y., Ma, Z. & Bruce, P. G. Ordered mesoporous metal oxides: Synthesis and applications. *Chem. Soc. Rev.* **41**, 4909–4927 (2012).

8. Xie, Y. & Fang, X. Electrochemical flexible supercapacitor based on manganese dioxide-titanium nitride nanotube hybrid. *Electrochim. Acta* **120**, 273–283 (2014).

9. Meher, S. K. & Rao, G. R. Enhanced activity of microwave synthesized hierarchical MnO_2 for high performance supercapacitor applications. *J. Power Sources* **215**, 317–328 (2012).

10. Toupin, M., Brousse, T. & Bélanger, D. Charge storage mechanism of MnO_2 electrode used in aqueous electrochemical capacitor. *Chem. Mater.* **16**, 3184–3190 (2004).

11. Lee, H. Y. & Goodenough, J. B. Supercapacitor behavior with KCl electrolyte. *J. Solid State Chem.* **144**, 220–223 (1999).

12. Zhu, J. *et al.* Oxidation-etching preparation of MnO_2 tubular nanostructures for high-performance supercapacitors. *ACS Appl. Mater. Interfaces* **4**, 2769–2774 (2012).

13. Li, H., Zhang, X., Ding, R., Qi, L. & Wang, H. Facile synthesis of mesoporous MnO_2 microspheres for high performance AC// MnO_2 aqueous hybrid supercapacitors. *Electrochim. Acta* **108**, 497–505 (2013).

14. Brousse, T. *et al.* Crystalline MnO_2 as possible alternatives to amorphous compounds in electrochemical supercapacitors. *J. Electrochem. Soc.* **153**, A2171 (2006).

15. Ghodbane, O., Pascal, J. L. & Favier, F. Microstructural effects on charge-storage properties in MnO_2-based electrochemical supercapacitors. *ACS Appl. Mater. Interfaces.* **1**, 1130–1139 (2009).

16. Zhang, Y. *et al.* Defect promoted capacity and durability of N-MnO2−x branch arrays via low-temperature NH3 treatment for advanced aqueous zinc ion batteries. *Small* **15**, 1905452 (2019).

17. Li, K. *et al.* Tuning MnO_2 to FeOOH replicas with bio-template 3D morphology as electrodes for high performance asymmetric supercapacitors. *Chem. Eng. J.* **370**, 136–147 (2019).

18. Li, K. *et al.* Assembling a double shell on a diatomite skeleton ternary complex with conductive polypyrrole for the enhancement of supercapacitors. *Chem. Commun.* **55**, 13773–13776 (2019).

19. Wang, T. *et al.* Tuning parallel manganese dioxide to hollow parallel hydroxyl oxidize iron replicas for high-performance asymmetric supercapacitors. *J. Colloid Interface Sci.* **594**, 812–823 (2021).

20. Li, K. *et al.* A multidimensional rational design of nickel–iron sulfide and carbon nanotubes on diatomite via synergistic modulation strategy for supercapacitors. *J. Colloid Interface Sci.* **603**, 799–809 (2021).

21. Huang, M. *et al.* MnO_2-based nanostructures for high-performance supercapacitors. *J. Mater. Chem. A* **3**, 21380–21423 (2015).

22. Huang, M. *et al.* Facile synthesis of hierarchical Co_3O_4@ MnO_2 core–shell arrays on Ni foam for asymmetric supercapacitors. *J. Power Sources* **252**, 98–106 (2014).

23. Li, F. *et al.* On-chip 3D interdigital micro-supercapacitors with ultrahigh areal energy density. *Energy Storage Mater.* **27**, 17–24 (2020).

24. Le, Q. J. *et al.* Biotemplate derived three dimensional nitrogen doped graphene@ MnO_2 as bifunctional material for supercapacitor and oxygen reduction reaction catalyst. *J. Colloid Interface Sci.* **544**, 155–163 (2019).

25. Liu, C., Zhang, Z. & Chen, L. Novel [111] oriented γ-Mo_2N thin films deposited by magnetron sputtering as an anode for aqueous micro-supercapacitors. *Electrochim. Acta* **245**, 237–248 (2017).

26. Das, B., Behm, M., Lindbergh, G., Reddy, M. V. & Chowdari, B. V. R. High performance metal nitrides, MN (M= Cr, Co) nanoparticles for non-aqueous hybrid supercapacitors. *Adv. Powder Technol.* **26**, 783–788 (2015).

27. Śliwak, A., Moyseowicz, A. & Gryglewicz, G. Hydrothermal-assisted synthesis of an iron nitride–carbon composite as a novel electrode material for supercapacitors. *J. Mater. Chem. A* **5**, 5680–5684 (2017).

28. Dong, S. *et al.* Facile preparation of mesoporous titanium nitride microspheres for electrochemical energy storage. *ACS Appl. Mater. Interfaces* **3**, 93–98 (2011).

29. Lin, Y. H., Li, J. Y., Ren, P. & Yang, C. C. $NH_4V_4O_{10}$ nanobelts vertically grown on 3D TiN nanotube arrays as high-performance electrode materials of supercapacitors. *RSC Adv.* **11**(15), 8468–8474 (2021).

30. Li, J. Y., Wu, R. & Yang, X. C. MoS_2 modified TiN nanotube arrays for advanced supercapacitors electrode. *Physica E* **118**(6), 113951 (2020).

31. Tang, S. *et al.* Preparation of Titanium nitride nanomaterials for electrode and application in energy storage. *Results Phys.* **7**, 1198–1201 (2017).

32. Zhang, X., Gang, Wu. & Yang, X.-C. MoS2 nanosheet-carbon foam composites for solar steam generation. *ACS Appl. Nano Mater.* **3**, 9706–9714 (2020).

33. Chen, C. & Yang, X. MnO_2 modified TiN nanotube arrays on Ti mesh for flexible supercapacitors electrode. *RSC Adv.* **7**, 56440–56446 (2017).

34. Truong, T. T., Liu, Y., Ren, Y., Trahey, L. & Sun, Y. Morphological and crystalline evolution of nanostructured MnO_2 and its application in lithium–air batteries. *ACS Nano* **6**, 8067–8077 (2012).

35. Wang, X. & Li, Y. Rational synthesis of α-MnO_2 single-crystal nanorods. *Chem. Commun.* **7**, 764–765 (2002).

36. Xiao, W., Wang, D. & Lou, X. W. Shape-controlled synthesis of MnO_2 nanostructures with enhanced electrocatalytic activity for oxygen reduction. *J. Phys. Chem. C* **114**, 1694–1700 (2010).

37. Subramanian, V., Zhu, H., Vajtai, R., Ajayan, P. M. & Wei, B. Hydrothermal synthesis and pseudocapacitance properties of MnO_2 nanostructures. *J. Phys. Chem. B* **109**, 20207–20214 (2005).

Acknowledgements

Author contributions

P.R. and C.C. contributed equally to this work. P.R. and C.C. performed experimental measurements; P.R. and C.C. performed the analysis and prepared figures, X.Y. designed, directed the work, and wrote the main manuscript text. All authors reviewed the manuscript.

Competing interests

The authors declare no competing interests.

Additional information

Correspondence and requests for materials should be addressed to X.Y.